

pubs.acs.org/JPCL Letter

Activation of N₂ on Manganese Nitride-Supported Ni₃ and Fe₃ Clusters and Relevance to Ammonia Formation

Bin Liu,* Narges Manavi, Hao Deng, Chaoran Huang, Nannan Shan, Viktor Chikan, and Peter Pfromm



Cite This: J. Phys. Chem. Lett. 2021, 12, 6535-6542



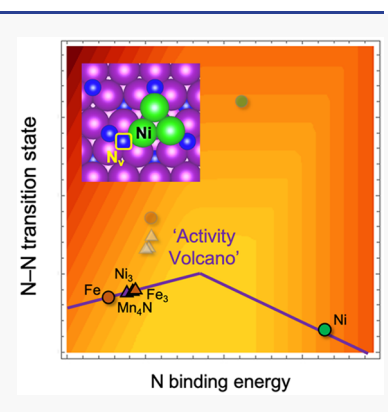
ACCESS

Metrics & More

Article Recommendations

Supporting Information

ABSTRACT: Dual-site models were constructed to represent manganese nitride (Mn_4N) -supported Ni_3 and Fe_3 clusters for NH_3 synthesis. Density functional theory calculations produced an energy barrier of approximately 0.55 eV for N-N bond activation at the interfacial nitrogen vacancy sites (N_v) ; also, the hydrogenation and removal of interfacial N is promoted by earth-abundant Ni and Fe metals. Steady-state microkinetic modeling revealed that the turnover frequencies of NH_3 production follow an order of $Fe_3@Mn_4N \approx Ni_3@Mn_4N > Mn_4N > Fe \gg Ni$. Moreover, we present clear evidence that, before NH_3 formation, NH migrates from N_v onto the metallic sites. Using N binding energy (BE_N) and the transition-state energy of N_2 activation (E_{TS}) as descriptors, we concluded that the beneficial effects owing to interfacial N_v sites are the most pronounced when BE_N is either too strong or too weak while E_{TS} is high; otherwise, excessive N_v sites may hinder catalyst performance.



lobal annual ammonia (NH₃) production is expected to grow to nearly 290 million metric tons by 2030.¹ Moreover, NH₃ is also considered as a feasible hydrogen storage and transportation carrier thanks to its high hydrogen content (17.7 wt % versus liquefied H₂) and high energy density (3 kWh/kg).²⁻⁵ To overcome the costly energy consumptions for NH₃ production, catalytic materials enabling alternative NH₃ synthesis routes (e.g., enzyme catalysis, electrocatalysis, nonthermal plasma, and chemical looping 10,11 are being actively explored. The catalytic performance of transition metals (TMs), metallic alloys, and metalloid derivatives (e.g., nitrides) have been extensively analyzed over decades of research.

An established principle dictating optimal NH₃ production rates emphasizes that the nitrogen binding energy descriptor can be neither too weak nor too strong. Theoretical works also highlighted that N–N bond activation and adsorptions of N are bounded by a reliable linear relationship. Hence, the performance of many NH₃ catalysts is intrinsically limited by these linear relationships. One way to circumvent such limitations would be to stabilize the transition state (i.e., lower the N–N activation energy barrier) without overbinding the NH_x (x = 1-3) intermediates. Work by Montoya and coworkers suggested that N₂-to-NH₃ conversions disobeying linear scaling relationships would be supported by multicomponent materials bearing distinct structural and chemical functionalities.

There is strong evidence that TMs or TM nitrides (e.g., Cr, Mn, Co, Ni, and Mn₄N) supported on alkali and alkaline earth hydrides (e.g., LiH, KH, CaH₂, and BaH₂) enable NH₃ formation at lower temperatures and near atmospheric pressure. 15,16 Chen and co-workers showed that Fe-LiH, Cr-

LiH, Mn-LiH, Co-LiH, Mn_4N -LiH, and Mn_4N -BaH₂ are all capable of boosting NH_3 production to varying degrees, ^{15,16} mainly because LiH hydride favors the formation of Li_2NH by utilizing the N supplied by the TM component.

Supports can also be exploited for N_2 activation. The instance, transition metals (e.g., Ru) on electride supports (e.g., Ca2N:e⁻¹⁹ and C12A7:e⁻¹⁷) exhibit lower work functions favoring N_2 activation. YN, LaN, and CeN also readily produce N vacancies (N_v) under NH₃ synthesis conditions. As illustrated in Scheme 1, these nitride supports adopt the roles in N_2 activation instead. Most recently, Ye and co-workers demonstrated that the rate of NH₃ production rate exceeds $5 \times 10^3 \, \mu \mathrm{mol} \, \mathrm{g}^{-1} \, \mathrm{h}^{-1}$ when Ni nanoparticles (12.5 wt %) are loaded on LaN. In the support of the role of the role of the rate of NH₃ production rate exceeds $5 \times 10^3 \, \mu \mathrm{mol} \, \mathrm{g}^{-1} \, \mathrm{h}^{-1}$ when Ni nanoparticles (12.5 wt %) are loaded on LaN.

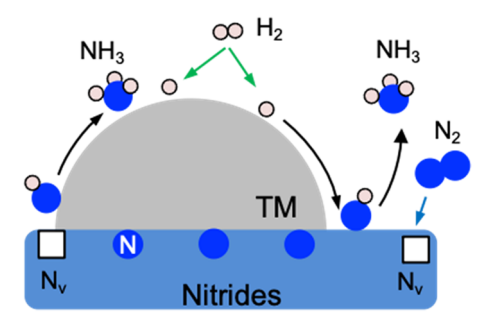
In this Letter, we report the investigation of a two-component model system consisting of earth-abundant transition metals (Ni and Fe) from group VIII on Mn_4N support. Manganese (Mn) is a notable N carrier and readily forms stable nitrides (Mn_4N), although a metastable $Mn_6N_{2.58}$ (the N-rich phase) can also be obtained at a temperature window between 700 and 800 °C.²⁴ It has already been shown that the rate of NH_3 production can be boosted using Mn_4N along with LiH.¹⁶ In addition to Fe that is a known NH_3 synthesis catalyst, we also deliberately chose Ni, which is much

Received: June 3, 2021 Accepted: July 7, 2021 Published: July 9, 2021





Scheme 1. Multicomponent Catalyst Models for NH₃ Formation^a



^aBlue and green arrows indicate N_2 and H_2 adsorptions; black arrows indicate directions of surface diffusion and NH_3 formation. N, N_v , and H species in the support are also labeled.

less active by itself because of weak N binding. However, H favors Ni surfaces and is quite mobile. Therefore, this choice may allow us to better understand the relation between $N_{\rm v}$ and different metal sites. In fact, Ni supported on BaH_2 has been reported to promote NH_3 production by an order of magnitude by facilitating H_2 activation. 25

Here, a simple TM-on-nitride dual-site model (Scheme 1) was investigated using density functional theory (DFT) to identify the roles of respective metal and interfacial $N_{\rm v}$ sites for H_2 and N_2 activations. Also, the most plausible NH_3 formation pathway on this dual-site configuration was elucidated. Lastly, the catalytic performance was assessed with a microkinetic model adapted specifically for the proposed dual-site systems.

The Mn₄N phase has a face-centered cubic (FCC) lattice, 26,27 with the lattice constant of 3.74 Å 28 (versus 3.86 Å measured experimentally 27). The Mn₄N support is represented by a semiperiodic 4-layer $p(2 \times 2)$ supercell slab, with the N-terminated facet along the (111) orientation. Four lattice N atoms (in blue) are exposed in the top layer within this supercell (Figure 1a). The bottom two layers are

fixed to the optimized bulk value. A 25 Å vacuum was added to separate the slab from its periodic images.

A three-atom Ni₃ cluster in an equilateral geometry ($d_{N_i-N_i}$ = 2.38 Å) was chosen to represent the metallic Ni sites anchored by three lattice N atoms in their native lattice positions (Figure 1a). Configurations depicting other Ni₃ arrangements are also shown in Figure S1. This triangular configuration is favored as Ni_3 maximizes its contact with the exposed lattice N (d_{Ni-N} = 1.83 Å) as anchor points. The optimized $d_{N_i-N_i}$ is 4% shorter than in Ni(111) (2.48 Å). The interatomic distance between the lattice N in the Ni₃-decorated Mn₄N is 5.29 Å (indicated by the double-headed arrow), versus 5.30 Å in plain $Mn_4N(111)$. A small contraction of d_{Ni-Ni} is normal in small clusters,²⁹ hinting that Ni₃ can fit comfortably among the toplayer lattice N with little external strain. The projected d-band of Ni₃ shifts slightly away from the Fermi level relative to Ni(111) (Figure 1b), a trend consistent with the d-band centers, i.e., -1.58 eV versus -0.37 eV between Ni₃ and Ni(111).

The interfacial nitrogen vacancy (N_v) is formed by removing one anchoring lattice N. The formation energy of interfacial N_v is 1.57 eV (endothermic), versus 1.64 eV for N_v formation in plain $Mn_4N(111)$, suggesting that Ni_3 may somewhat destabilize the anchoring N through the metal—support-type interaction. The prevalence of the targeted N_v sites was also determined from thermodynamic calculations (see the Supporting Information for computational details), which revealed that the removal of hydrogenated anchoring N (as NH) is only moderately endothermic (0.38 eV) at 773 K and 2 bar and will be exogenic at even higher temperatures (e.g., 973 K). Hence, the proposed $Ni_3@Mn_4N$ structure in principle can be "activated" at elevated temperatures prior to NH_3 synthesis in a hydrogen environment.

On $Mn_4N(111)$ with an N_v site (Figure 2a), a stable molecular N_2 adsorption state (IS) exists with a binding energy of -1.03 eV. In the N_2 activation transition state (TS), the N-N bond is stretched to 1.83 Å, yielding an energy barrier of 0.65 eV. Upon activation, the N_v site is fulfilled with one

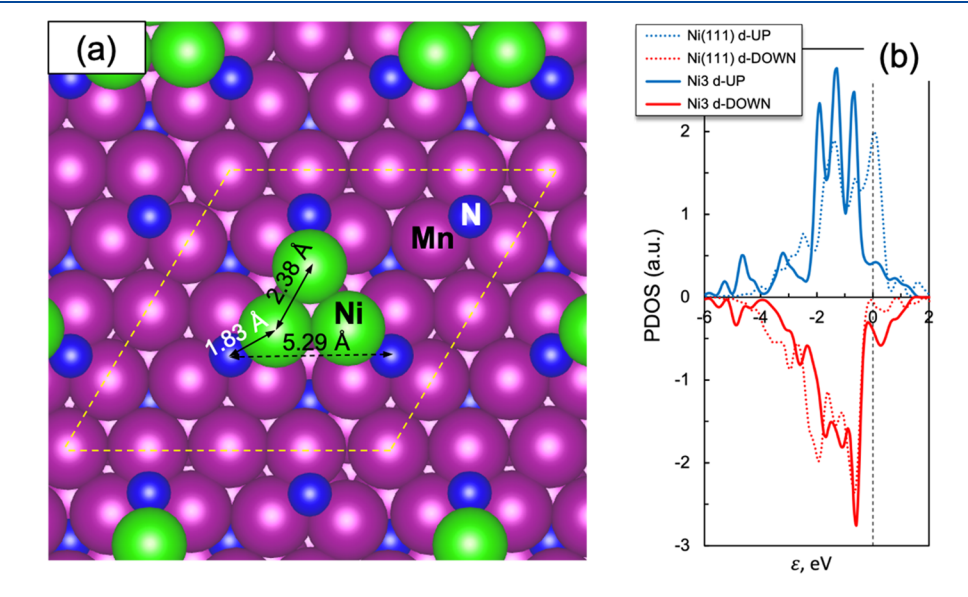


Figure 1. (a) Optimized $Ni_3@Mn_4N$ in a $p(2 \times 2)$ supercell. The cell boundaries are indicated by yellow dashed lines. The N, Mn, and Ni atoms are in blue, purple, and green, respectively. The Ni–Ni, N–Ni, and N–N bond distances are also indicated with black arrows. (b) Projected density of states (PDOS) of Ni atoms in $Ni_3@Mn_4N$ (solid lines) versus Ni(111) (dotted lines): spin-up (blue) and spin-down (red). The Fermi level is indicated by the vertical dashed line.

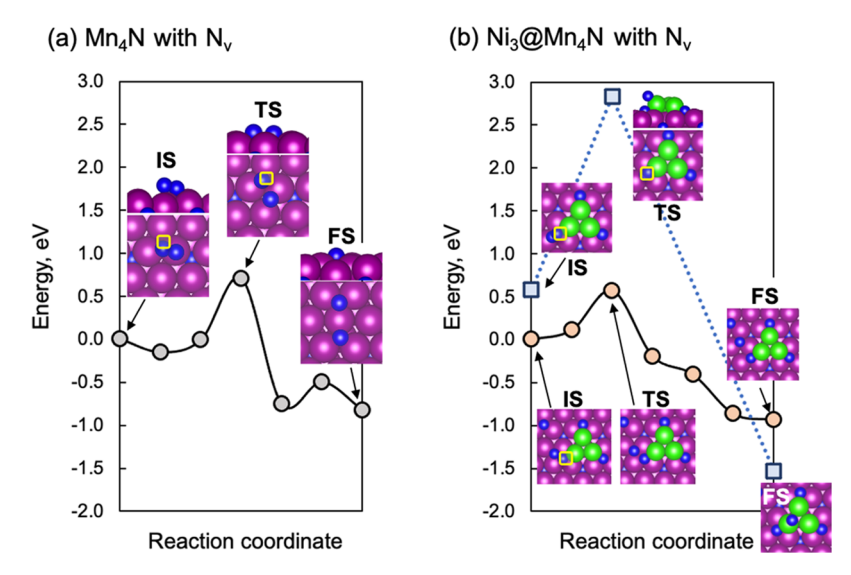


Figure 2. N_2 activation on the N_v site in (a) $Mn_4N(111)$ and (b) $Ni_3@Mn_4N(111)$. The initial state (IS), transition state (TS), and final state (FS) are labeled. In panel b, the lower N_2 adsorption energy state (i.e., IS) was chosen as the zero-energy reference. The higher-energy pathway (i.e., N_2 activation at the Ni site) is shown in blue dotted lines. N_v sites are indicated by yellow squares.

dissociated N, while the other N is located at a nearby 3-fold site. The final state (FS) is in a lower-energy state (-0.82 eV). On the Ni₃-decorated Mn₄N, molecular N₂ binds at the interfacial N_v site with a comparable binding energy of -0.99 eV. Illustrated by the inset figure (or Figure S2F), one N atom occupies the N_v site (yellow square), while the other N atom stays on the Mn₄N substrate. Metastable N₂ adsorption states also exist with weaker binding energies, such as -0.11 eV in Figure S2D and -0.41 eV in Figure S2F. In the absence of N_v, N₂ would favor the Ni site and prefers the bridge location between two Ni atoms (Figure S2B). Still, all binding energies in Figure S2A–C are weaker than at the N_v site illustrated in Figure S2F.

 N_2 activation following the low potential energy profile on Ni_3 -decorated Mn_4N (solid black in Figure 2b) resembles that on $Mn_4N(111)$. An energy barrier of 0.55 eV was determined from the CI-NEB calculations, with a N–N distance of 1.71 Å in the TS. This barrier is even lower than on the plain $Mn_4N(111)$ but slightly higher than on Ru (0.4 eV),³⁰ one of the most active NH_3 synthesis catalysts.

The high-energy N_2 dissociation pathway (dashed blue in Figure 2b) shows a metastable N_2 adsorption state at the interfacial N_v site as the IS. However, the N–N activation occurs on the corner Ni atom in Ni₃, producing one N atom filling the N_v site and a second N atom migrating on top of Ni₃. The effective energy barrier is 2.3 eV, which is significantly higher despite being more exothermic (–1.53 eV for FS). This comparison makes it clear that the occurrence of N_2 activation at the Ni site is unlikely.

Hydrogen atoms generally prefer the Ni site, with binding energies ranging from -0.9 to -1.0 eV (Figure S3). DFT calculations revealed that atomic H atom favors the 3-fold site on the Ni $_3$ cluster (Figure S3D), regardless of the presence of $N_{\rm v}$. Given this clear preference to the Ni site, H_2 activation will unlikely compete directly with N_2 activation taking place at the $N_{\rm v}$ site, enabling H_2 and N_2 activations to proceed without direct site competition.

As illustrated in Figure S4, H₂ activation initiates at the Ni top site, followed by H–H bond dissociation with an energy barrier of 0.19 eV. One of the dissociated H atoms remains at

the Ni sites. The H spillover results in H migration onto the anchoring N site. In this work, the H_2 dissociation kinetics shall be approximated as an equilibrated step.

 NH_3 formation proceeds through a series of stepwise hydrogenation steps that convert the anchor N atoms at the interfacial N_v sites into NH_3 . For both Ni_3 - and Fe_3 -decorated Mn_4N , we adopted the following NH_3 formation pathways (R1–R9) involving N_v and metal sites:

$$N_2(g) + 2 \overline{\square} \leftrightarrow N_2^{\#} \to 2N^{\overline{\square}}$$
 (R1)

$$H_2(g) + * \leftrightarrow 2H^* \tag{R2}$$

$$N^{\Box} + H^* \leftrightarrow NH^{\Box} \tag{R3}$$

$$NH^{\odot} + H^* \leftrightarrow NH_2^{\odot}$$
 (R4)

$$NH_2^{\odot} + H^* \leftrightarrow NH_3(g) + \odot + *$$
 (R5)

$$NH^{\square} \leftrightarrow NH^*$$
 (R6)

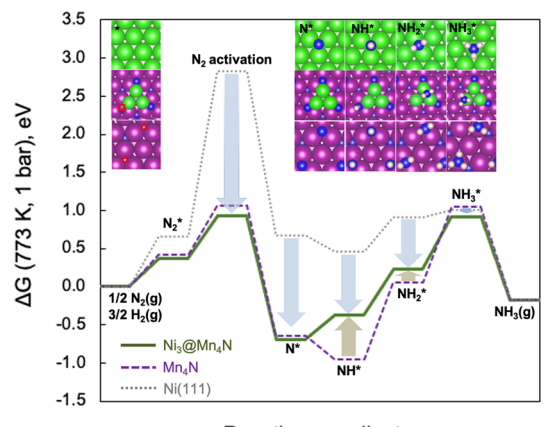
$$NH^* + H^* \leftrightarrow NH_2^* \tag{R7}$$

$$NH_2^{\odot} \leftrightarrow NH_2^*$$
 (R8)

$$NH_2^* + H^* \leftrightarrow NH_3(g) + 2^*$$
 (R9)

The interfacial N_v site and the metal (Ni or Fe) site are denoted as " \boxdot " and "*", respectively. N_2 and H_2 activations will occur only at the respective \boxdot and * sites. Steps distinguishing the dual-site mechanism are R3, R4, R5, R6, and R8. NH_x (x=1-3) formation may occur with NH_x (x=0-2) at the interfacial N_v site and H at the metal site, as in R3-R5. In addition, we allow diffusions of NH and NH_2 between \boxdot and * sites, as in R6 and R8. These steps are included because DFT calculations suggest that there is no clear site preference for NH and NH_2 between \boxdot and * sites. The final NH_3 formation and desorption liberating the active sites (both \boxdot and *) are represented by R5 and R9. Similar dual-site mechanisms for NH_3 formation have been discussed by Mehta⁹ and Vojvodic. ³¹

The Gibbs free-energy profiles depicting NH_3 formation at 773 K are displayed in Figure 3. On Ni_3 -decorated Mn_4N



Reaction coordinate

Figure 3. Free-energy profiles (at 773 K) depicting NH₃ formation on Ni₃@Mn₄N (green solid), Ni(111) (gray dotted), and Mn₄N(111) (purple dashed). The blue and beige arrows indicate the shift of the free energies at certain steps for respective Ni and Mn₄N relative to Ni₃@Mn₄N. The surface and interfacial N_v sites on respective Mn₄N(111) and Ni₃@Mn₄N are displayed as red triangles and square. The configurations for N*, NH*, NH₂*, and NH₃* intermediates are also shown in the inset figures. The H, N, Ni, and Mn atoms are depicted in white, blue, green, and magenta, respectively.

(solid green), the initial N_2 activation proceed along an energy uphill to overcome the entropy loss and the N–N bond activation energy barrier, filling interfacial $N_{\rm v}$ site. Afterward, successive NH, NH $_2$, and NH $_3$ formation steps are endergonic as well, followed by an energy drop associated with NH $_3$ desorption due to large entropy gain. The combined N_2 adsorption and activation process indicate R1 as the rate-

limiting step. However, the hydrogenation steps may also hinder the rate of NH_3 formation, as for Mn_4N and $Ni_3\text{-}$ decorated $Mn_4N.^{32}$

On plain Mn₄N(111) (dashed purple), the free-energy profile for N₂ activation regular N_v sites follows closely the interfacial N_v sites. As discussed earlier, the N-N activation barrier is slightly higher than on the Ni_3 -decorated $\mathrm{Mn}_4\mathrm{N}.$ The most notable distinction is related to NH formation. NH binds stronger at the N_v site in Mn₄N(111); as such, the conversion of lattice N into NH is exergonic (Figure 3), making NH a likely MASI (i.e., most abundant surface intermediate) on Mn₄N(111). The consequence is that subsequent hydrogenation steps leading to NH3 formation will be slowed down. Hence, there is an advantage for N2 activation to take place at the interfacial N_v sites, as subsequent conversions of NH become easier over a regular N_v in Mn₄N (highlighted by the beige arrows). On Ni(111), we confirmed that the N₂ activation energy barrier (2.16 eV) is just too high for pure Ni to be competitive against the other two systems.

The Fe₃-decorated Mn₄N, denoted as Fe₃@Mn₄N, was built as a structural analog to Ni₃@Mn₄N (Figure S5). The favored Fe₃ configuration also exhibits an equilateral triangular geometry anchored by three lattice N atoms. The measured $d_{\text{Fe-Fe}}$ is 2.41 Å, a slightly larger (6.2%) contraction from the FCC Fe lattice (2.57 Å). The distance between two anchoring N atoms is 5.33 Å, again, also showing little strain for Fe₃ accommodation. Atomic N binds stronger on metallic Fe. On Fe₃@Mn₄N, N₂ (Figure S6B) and N (Figure S6D) both prefer the Fe site even in the presence of interfacial N_v. A direct comparison of the free-energy profiles (Figure S7) suggests that the difference for R1 between Ni₃@Mn₄N and Fe₃Mn₄N is negligible. However, all NH_x (x = 1-3) show site preference to the Fe sites over N_v (see inset figures of Figure S7) to such an extent that NH formation at the Fe site is exergonic as on

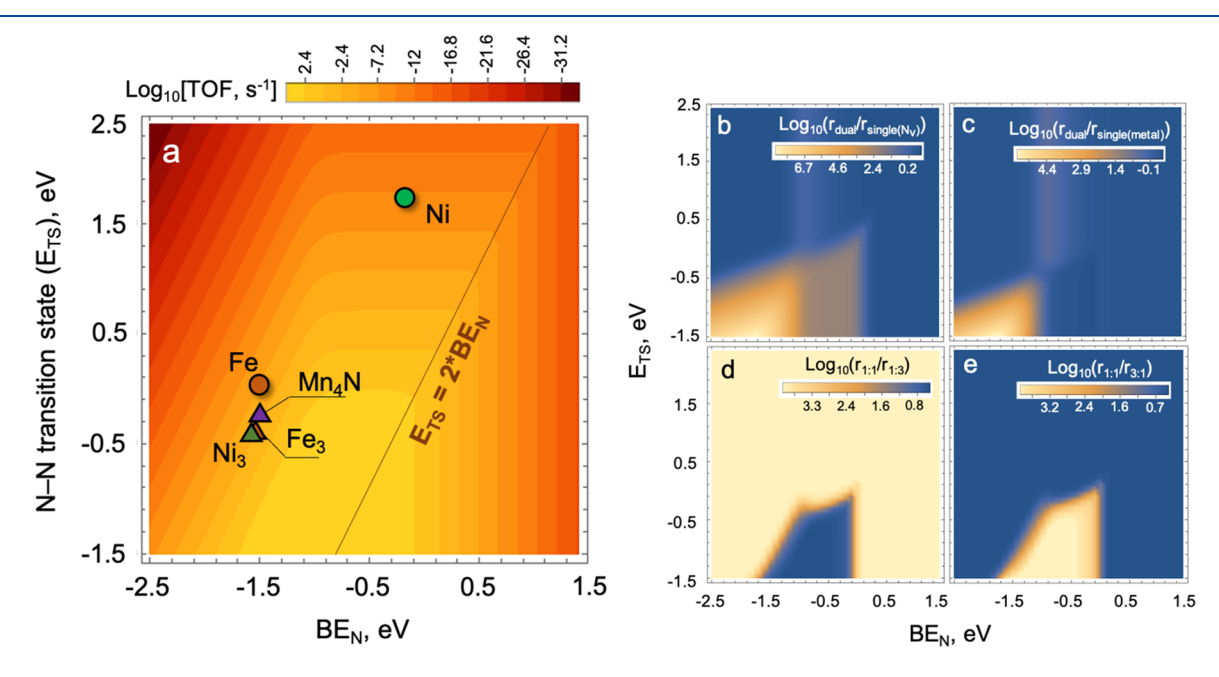


Figure 4. (a) Turnover frequencies for NH₃ production (Log₁₀[TOF, s⁻¹]) at an N_v:Ni(Fe) site ratio of 1:1. The locations of Ni₃@Mn₄N (green triangle), Fe₃@Mn₄N (orange triangle), Mn₄N(111) (purple triangles), Fe(111) (orange dot), and Ni(111) (green dot) are indicated in the plot. (b) Relative performance gain due to the synergy between N_v and metal sites (Log₁₀[$r_{dual}/r_{single(N_v)}$]) over N_v single-site. (c) Relative performance again (Log₁₀[$r_{dual}/r_{single(N_v)}$) over metal single-site. (d) Relative performance against 1:3 N_v:Ni/Fe site ratio. (e) Relative performance against 3:1 N_v:Ni/Fe site ratio. All modelings were performed at 773 K, 0.5 bar of N₂, 1.5 bar of H₂, and trace amount of NH₃.

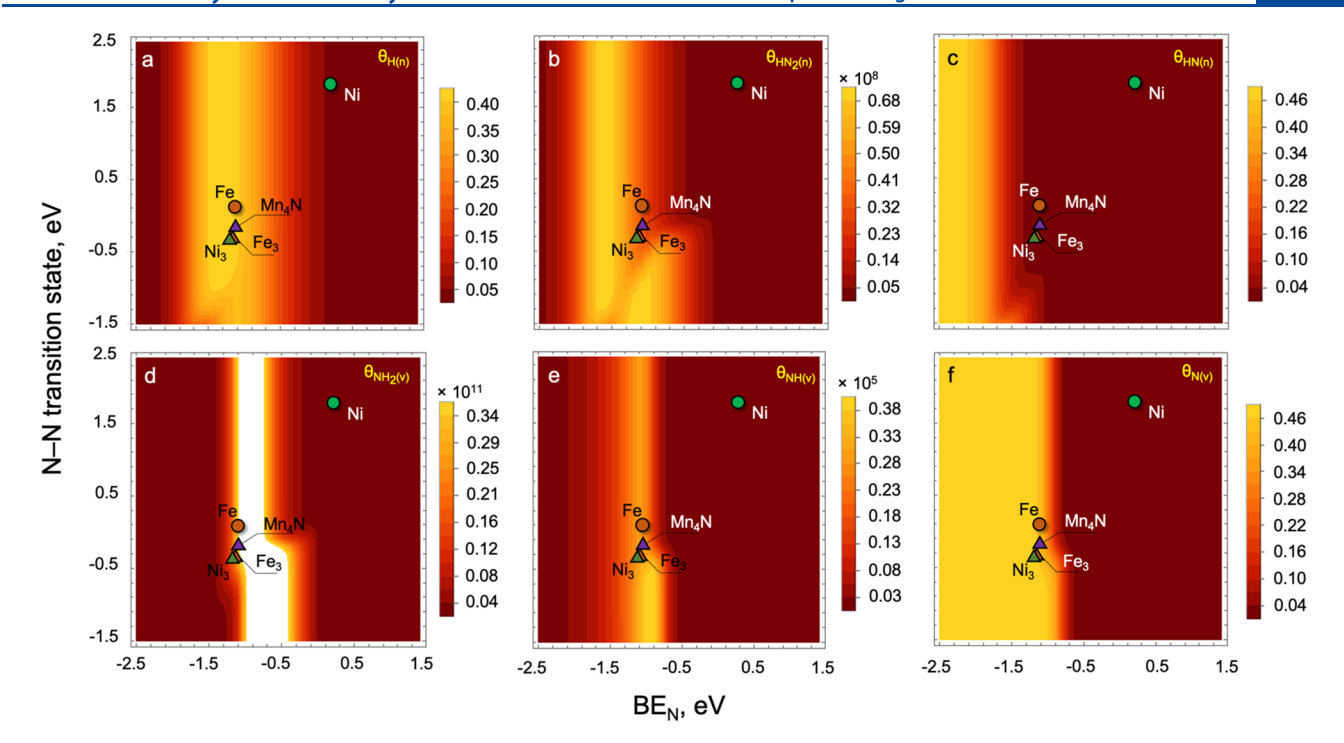


Figure 5. Surface intermediates coverage for (a) H (at metal site), (b) NH_2 (at metal site), (c) NH (at metal site), (d) NH_2 (at N_v site), (e) NH (at N_v site), and (f) N (at N_v site). Locations of $Ni_3@Mn_4N$, $Fe_3@Mn_4N$, $Mn_4N(111)$, Ni(111), and Fe(111) are also labeled in each plot.

plain $Mn_4N(111)$. NH_2 and NH_3 formations at the Fe sites remain endogenic.

The newly calculated BE_N and BE_{NH_x} for $Ni_3@Mn_4N$ and $Fe_3@Mn_4N$ (magenta crosses in Figure S8) were added to the linear relationship established in our previous work. The BE_{NH} of $Ni_3@Mn_4N$ is located well above the linear correlation (Figure S8a), indicating substantial destabilization of NH at the interfacial N_v site, whereas BE_{NH} on $Fe_3@Mn_4N$ does not appear to deviate from the main correlation. BE_{NH_2} on $Ni_3@Mn_4N$ and $Fe_3@Mn_4N$ both lie in the proximity of the linear correlation (Figure S8b). Moreover, NH_3 binding (BE_{NH_3}) at the Fe site will be stronger than the linear correlation prediction (Figure S8c). Overall, the destabilization of NH on $Ni_3@Mn_4N$ and overbinding of NH_3 on $Fe_3@Mn_4N$ were identified to violate the linear scaling relationships. However, it is the NH destabilization that will be more likely to benefit NH_3 formation.

The turnover frequencies (TOFs) for NH₃ production, as $Log_{10}[TOF]$, were obtained using CatMAP³³ as the numerical solutions to the reaction scheme following R1-R9 at 773 K and an absolute pressure of 2 bar. The NH₃ production rates are displayed using the two established descriptors: BE_N (binding energy of N) and E_{TS} (transition-state energies of N-N activation).

Figure 4a confirms the existence of the well-known *volcano* shape dictated by the Sabatier principle, ¹³ even within a dual-site mechanism. Specifically, $\text{Log}_{10}[\text{TOF}]$ follows a decreasing order of $\text{Fe}_3 @ \text{Mn}_4 \text{N} \approx \text{Ni}_3 @ \text{Mn}_4 \text{N} > \text{Mn}_4 \text{N} > \text{Fe} \gg \text{Ni}$. If Fe is used as the benchmark for catalyst performance, NH₃ production TOFs improve on all Mn₄N-based systems owing to lower N–N activation transition-state energies at similar or even lower BE_N than on Fe. For Mn₄N-based catalysts, it is likely that their E_{TS} and BE_N may not follow the same Brønsted–Evans–Polanyi (BEP) relationship previously estab-

lished for simple TM systems, 31,34 a desirable outcome being actively pursued in the NH₃ catalyst design paradigm.

Catalytic performance gains in bifunctional catalysis were analyzed by Andersen et al. using generic BEP relationships.³⁵ In this work, the performance gains in NH3 production were evaluated using concrete synergistic dual-site systems in terms of $\text{Log}_{10}[r_{\text{dual}}/r_{\text{single}}]$. Two single-site systems with uniform N_{v} or metal active sites, which are distinguished by their respective linear scaling relationships for BE_{NH} and BE_{NH}, (see eqs S3–S6 in Appendix 1 of the Supporting Information), were also considered. Compared to N_v-based single-site catalysts (Figure 4b), the most significant performance gains are achieved for the scenario with strong BE_N and low E_{TS} . According to Scheme 1, the advantage provided by dual-site systems is their ability to convert and transport MASI species with the assistance of the second site, which is realized by R6. For systems with uniform metallic sites, a similar phenomenon was observed (Figure 4c). Nevertheless, influenced by the linear scaling relationships of metallic systems,³⁶ the performance gains are generally diminished. When either BE_N or E_{TS} becomes higher, the single-site metallic catalysts may outperform the Mn₄N-based dual-site systems. Figure 4c indicates that when dual-site nitrides are unable to support fast N₂ activation at strong N binding, a strong correlation between BE_{N} and BE_{NH}^{32} will likely hinder NH_{3} production instead.

The high degree of consistency between the numerical modeling and DFT calculations (Figures 3 and S7) present convincing evidence that the modeled dual-site systems will boost the rates of NH $_3$ production. In fact, we anticipate that an even higher performance gain can be achieved according to the heatmap presented in Figure 4a, for instance, by further lowering $E_{\rm TS}$, or increasing BE $_{\rm N}$, or both. However, this will likely require more drastic measures to break the linear scaling relationships.

At a steady state, the most common surface intermediates on $Ni_3@Mn_4N$ and $Fe_3@Mn_4N$ (with a 1:1 N_v :Ni/Fe ratio) are revealed to be H at the metal site (Figure 5a) and N at the N_v site (Figure 5f). In comparison, the occupations by NH (Figure 5e) and NH₂ (Figure 5d) at the interfacial N_v site are orders of magnitudes lower than N. Interestingly, a small but not negligible amount of NH can be identified at the metal site (Figure 5c), where NH₂ (Figure 5b) remains negligible. Because only NH and NH₂ migrations (R6 and R8) were considered in the proposed dual-site mechanism, it can be concluded that NH is first formed at the N_v site, followed by migration to the metal (Ni and Fe) site. As such, NH migration (R6) supplies the feedstock for NH₃ formation while freeing N_v sites. It can be said that this mechanism becomes feasible because of the synergy within the dual-site systems.

Lastly, the relative performance gains due to the variations of the N_v :Ni/Fe site ratio were considered. Two scenarios, $Log_{10}[r_{1:1}/r_{1:3}]$ and $(Log_{10}[r_{1:1}/r_{3:1}])$ for N_v :Ni/Fe = 1:3 and 3:1, were adopted to represent systems with more abundant metal (Figure 4d) or N_v site (Figure 4e), respectively. For metal site-rich systems, gains were observed broadly except for the lower central region (Figure 4d), suggesting that the catalyst performance is limited by an N_v deficiency when BE_N is too strong or weak and/or that E_{TS} becomes higher. When N_v outnumbers the metal sites, gains will be concentrated in the lower central region (Figure 4e), suggesting that for too strong or weak BE_N , and/or high E_{TS} , the performance will not improve significantly (in the dark blue area). In fact, NH_3 production could be hindered for some systems (located in the yellow area in Figure 4e) with given excessive N_v sites.

These analyses have not only tested the limit of manganese nitride-based dual-site catalysts in boosting NH_3 formation but also posed an interesting optimization problem regarding the composition and active site structures of such dual-site systems. As the catalyst design paradigm for NH_3 synthesis catalysts continues to expand, higher N_2 activation capacity and new NH_3 formation pathways will be discovered and optimized in the future.

METHODS

Spin-polarized, periodic DFT calculations were performed using the Vienna Ab Initio Simulation Package (VASP), 37,38 in which the core electrons were described using the projectoraugmented wave (PAW) pseudopotential.³⁹ The plane-wave basis set was expanded up to a cutoff energy of 400 eV. The electron-electron exchange-correlation energies were determined with the GGA-PBE functional.⁴⁰ The reciprocal first Brillouin zone was sampled using a k-point mesh generated using the Monkhorst-Pack scheme. 41 Convergence tests showed that the total energies converge within 20 meV when a $2 \times 2 \times 1$ mesh is used. Self-interaction errors (SIEs) for the substrate (i.e., Mn₄N) were also investigated using Dudarev's GGA+U approach, 42 but the influence of U on both the structure and magnetic properties of Mn₄N is negligible.²⁸ Dipole corrections were included in all slab calculations. The energy barriers of N2 and H2 activation on the top layer were calculated using the climbing image nudged elastic band (CI-NEB)⁴³ and dimer methods.⁴⁴ Steady-state microkinetic model and numerical solutions (R1-R9) were performed at 773 K and 2 bar using the CatMAP program to obtain the rates of NH₃ production.³³ The modeling details are reported in the Supporting Information.

ASSOCIATED CONTENT

Supporting Information

The Supporting Information is available free of charge at https://pubs.acs.org/doi/10.1021/acs.jpclett.1c01752.

Molecular configurations of Ni $_3$ @Mn $_4$ N, Fe $_3$ @Mn $_4$ N, and adsorbates; H $_2$ dissociation pathway; NH $_3$ free-energy diagram on Ni $_3$ @Mn $_4$ N and Fe $_3$ @Mn $_4$ N; linear scaling relationships of NH, NH $_2$, NH $_3$, N $_v$ formation, and microkinetic modeling computational details (PDF)

NH₃ energies (TXT) Coupling file (TXT)

AUTHOR INFORMATION

Corresponding Author

Bin Liu — Tim Taylor Department of Chemical Engineering, Kansas State University, Manhattan, Kansas 66506, United States; oorcid.org/0000-0001-7890-7612; Email: binliu@ksu.edu

Authors

Narges Manavi — Tim Taylor Department of Chemical Engineering, Kansas State University, Manhattan, Kansas 66506, United States

Hao Deng – Tim Taylor Department of Chemical Engineering, Kansas State University, Manhattan, Kansas 66506, United States

Chaoran Huang — Tim Taylor Department of Chemical Engineering, Kansas State University, Manhattan, Kansas 66506, United States

Nannan Shan — Materials Science Division, Argonne National Laboratory, Lemont, Illinois 60439, United States; orcid.org/0000-0002-7700-6246

Viktor Chikan — Department of Chemistry, Kansas State University, Manhattan, Kansas 66506, United States; orcid.org/0000-0002-4157-3556

Peter Pfromm — Voiland School of Chemical Engineering and Bioengineering, Washington State University, Pullman, Washington 99164, United States; orcid.org/0000-0003-4869-9503

Complete contact information is available at: https://pubs.acs.org/10.1021/acs.jpclett.1c01752

Notes

The authors declare no competing financial interest.

ACKNOWLEDGMENTS

B.L. thanks Mingxia Zhou for help with the data conversion. B.L., P.P., and V.C. are grateful for the financial support provided by the U.S. Department of Energy, Office of Science, Office of DOE EPSCoR, under Award Number DOE EPSCoR DE-FOA-0001572. The authors are grateful for the supercomputing service provided by K-State Beocat Research Cluster funded in part by NSF Grants CHE-1726332, CNS-1006860, EPS-1006860, and EPS-0919443 and the National Energy Research Scientific Computing Center (NERSC) under Contract No. DE-AC02-05CH11231.

REFERENCES

(1) Garside, M. https://www.statista.com/statistics/1065865/ammonia-production-capacity-globally/.

- (2) Erisman, J. W.; Sutton, M. A.; Galloway, J.; Klimont, Z.; Winiwarter, W. How a Century of Ammonia Synthesis Changed the World. *Nat. Geosci.* **2008**, *1* (10), 636–639.
- (3) Liu, H. Ammonia Synthesis Catalyst 100 Years: Practice, Enlightenment and Challenge. *Chin. J. Catal.* **2014**, 35 (10), 1619–1640.
- (4) Pfromm, P. H. Towards Sustainable Agriculture: Fossil-Free Ammonia. *J. Renewable Sustainable Energy* **2017**, 9 (3), 034702.
- (5) Valera-Medina, A.; Amer-Hatem, F.; Azad, A. K.; Dedoussi, I. C.; de Joannon, M.; Fernandes, R. X.; Glarborg, P.; Hashemi, H.; He, X.; Mashruk, S.; et al. Review on Ammonia as a Potential Fuel: From Synthesis to Economics. *Energy Fuels* **2021**, *35* (9), 6964–7029.
- (6) Brown, K. A.; Harris, D. F.; Wilker, M. B.; Rasmussen, A.; Khadka, N.; Hamby, H.; Keable, S.; Dukovic, G.; Peters, J. W.; Seefeldt, L. C.; et al. Light-Driven Dinitrogen Reduction Catalyzed by a CdS:Nitrogenase MoFe Protein Biohybrid. *Science* **2016**, 352 (6284), 448–450.
- (7) Rosca, V.; Duca, M.; de Groot, M. T.; Koper, M. T. M. Nitrogen Cycle Electrocatalysis. *Chem. Rev.* **2009**, *109* (6), 2209–2244.
- (8) McEnaney, J. M.; Singh, A. R.; Schwalbe, J. A.; Kibsgaard, J.; Lin, J. C.; Cargnello, M.; Jaramillo, T. F.; Nørskov, J. K. Ammonia Synthesis from N₂ and H₂O Using a Lithium Cycling Electrification Strategy at Atmospheric Pressure. *Energy Environ. Sci.* **2017**, *10* (7), 1621–1630.
- (9) Mehta, P.; Barboun, P.; Herrera, F. A.; Kim, J.; Rumbach, P.; Go, D. B.; Hicks, J. C.; Schneider, W. F. Overcoming Ammonia Synthesis Scaling Relations with Plasma-Enabled Catalysis. *Nat. Catal.* **2018**, *1* (4), 269–275.
- (10) Gálvez, M. E.; Halmann, M.; Steinfeld, A. Ammonia Production via a Two-Step Al_2O_3/AlN Thermochemical Cycle. 1. Thermodynamic, Environmental, and Economic Analyses. *Ind. Eng. Chem. Res.* **2007**, 46 (7), 2042–2046.
- (11) Michalsky, R.; Avram, A. M.; Peterson, B. A.; Pfromm, P. H.; Peterson, A. A. Chemical Looping of Metal Nitride Catalysts: Low-Pressure Ammonia Synthesis for Energy Storage. *Chem. Sci.* **2015**, *6* (7), 3965–3974.
- (12) Nørskov, J. K.; Bligaard, T.; Rossmeisl, J.; Christensen, C. H. Towards the Computational Design of Solid Catalysts. *Nat. Chem.* **2009**, *1* (1), 37–46.
- (13) Medford, A. J.; Vojvodic, A.; Hummelshøj, J. S.; Voss, J.; Abild-Pedersen, F.; Studt, F.; Bligaard, T.; Nilsson, A.; Nørskov, J. K. From the Sabatier principle to a predictive theory of transition-metal heterogeneous catalysis. *J. Catal.* **2015**, 328, 36–42.
- (14) Montoya, J. H.; Seitz, L. C.; Chakthranont, P.; Vojvodic, A.; Jaramillo, T. F.; Nørskov, J. K. Materials for solar fuels and chemicals. *Nat. Mater.* **2017**, *16* (1), 70–81.
- (15) Wang, P.; Chang, F.; Gao, W.; Guo, J.; Wu, G.; He, T.; Chen, P. Breaking Scaling Relations to Achieve Low-Temperature Ammonia Synthesis through LiH-Mediated Nitrogen Transfer and Hydrogenation. *Nat. Chem.* **2017**, *9* (1), 64–70.
- (16) Chang, F.; Guan, Y.; Chang, X.; Guo, J.; Wang, P.; Gao, W.; Wu, G.; Zheng, J.; Li, X.; Chen, P. Alkali and Alkaline Earth Hydrides-Driven N₂ Activation and Transformation over Mn Nitride Catalyst. *J. Am. Chem. Soc.* **2018**, *140* (44), 14799–14806.
- (17) Kitano, M.; Inoue, Y.; Yamazaki, Y.; Hayashi, F.; Kanbara, S.; Matsuishi, S.; Yokoyama, T.; Kim, S.-W.; Hara, M.; Hosono, H. Ammonia Synthesis Using a Stable Electride as an Electron Donor and Reversible Hydrogen Store. *Nat. Chem.* **2012**, *4* (11), 934–940.
- (18) Kitano, M.; Kanbara, S.; Inoue, Y.; Kuganathan, N.; Sushko, P. V.; Yokoyama, T.; Hara, M.; Hosono, H. Electride Support Boosts Nitrogen Dissociation Over Ruthenium Catalyst and Shifts the Bottleneck in Ammonia Synthesis. *Nat. Commun.* **2015**, *6* (1), 6731–6731.
- (19) Kitano, M.; Inoue, Y.; Ishikawa, H.; Yamagata, K.; Nakao, T.; Tada, T.; Matsuishi, S.; Yokoyama, T.; Hara, M.; Hosono, H. Essential Role of Hydride Ion in Ruthenium-Based Ammonia Synthesis Catalysts. *Chem. Sci.* **2016**, *7* (7), 4036–4043.

- (20) Hattori, M.; Iijima, S.; Nakao, T.; Hosono, H.; Hara, M. Solid Solution for Catalytic Ammonia Synthesis from Nitrogen and Hydrogen Gases at 50°C. *Nat. Commun.* **2020**, *11* (1), 2001–2008.
- (21) Ye, T.-N.; Park, S.-W.; Lu, Y.; Li, J.; Sasase, M.; Kitano, M.; Tada, T.; Hosono, H. Vacancy-Enabled N₂ Activation for Ammonia Synthesis on an Ni-loaded Catalyst. *Nature* **2020**, *583* (7816), 391–395.
- (22) Balasubramanian, K.; Khare, S. V.; Gall, D. Energetics of Point Defects in Rocksalt Structure Transition Metal Nitrides: Thermodynamic Reasons for Deviations from Stoichiometry. *Acta Mater.* **2018**, 159, 77–88.
- (23) Ye, T. N.; Park, S. W.; Lu, Y.; Li, J.; Sasase, M.; Kitano, M.; Hosono, H. Contribution of Nitrogen Vacancies to Ammonia Synthesis over Metal Nitride Catalysts. *J. Am. Chem. Soc.* **2020**, *142* (33), 14374–14383.
- (24) Heidlage, M. G.; Kezar, E. A.; Snow, K. C.; Pfromm, P. H. Thermochemical Synthesis of Ammonia and Syngas from Natural Gas at Atmospheric Pressure. *Ind. Eng. Chem. Res.* **2017**, *56* (47), 14014–14024.
- (25) Gao, W.; Guo, J.; Wang, P.; Wang, Q.; Chang, F.; Pei, Q.; Zhang, W.; Liu, L.; Chen, P. Production of Ammonia via a Chemical Looping Process Based on Metal Imides as Nitrogen Carriers. *Nat. Energy* **2018**, *3* (12), 1067–1075.
- (26) Takei, W. J.; Heikes, R. R.; Shirane, G. Magnetic Structure of Mn₁N-Type Compounds. *Phys. Rev.* **1962**, *125* (6), 1893–1897.
- (27) Fruchart, D.; Givord, D.; Convert, P.; l'Heritier, P.; Senateur, J. P. The Non-collinear Component in the Magnetic Structure of Mn_4N . J. Phys. F: Met. Phys. 1979, 9 (12), 2431.
- (28) Shan, N.; Chikan, V.; Pfromm, P.; Liu, B. Fe and Ni Dopants Facilitating Ammonia Synthesis on Mn4N and Mechanistic Insights from First-Principles Methods. *J. Phys. Chem. C* **2018**, *122* (11), 6109–6116.
- (29) Apai, G.; Hamilton, J. F.; Stohr, J.; Thompson, A. Extended X-Ray-Absorption Fine Structure of Small Cu and Ni Clusters: Binding-Energy and Bond-Length Changes with Cluster Size. *Phys. Rev. Lett.* **1979**, 43 (2), 165–169.
- (30) Logadóttir, Á.; Nørskov, J. K. Ammonia Synthesis Over a Ru(0001) Surface Studied by Density Functional Calculations. *J. Catal.* **2003**, 220 (2), 273–279.
- (31) Vojvodic, A.; Medford, A. J.; Studt, F.; Abild-Pedersen, F.; Khan, T. S.; Bligaard, T.; Nørskov, J. K. Exploring the limits: A low-pressure, low-temperature Haber-Bosch process. *Chem. Phys. Lett.* **2014**, *598*, 108–112.
- (32) Shan, N.; Huang, C.; Lee, R. T.; Manavi, N.; Xu, L.; Chikan, V.; Pfromm, P. H.; Liu, B. Manipulating the Geometric and Electronic Structures of Manganese Nitrides for Ammonia Synthesis. *Chem-CatChem* **2020**, *12* (8), 2233–2244.
- (33) Medford, A. J.; Shi, C.; Hoffmann, M. J.; Lausche, A. C.; Fitzgibbon, S. R.; Bligaard, T.; Nørskov, J. K. CatMAP: A Software Package for Descriptor-Based Microkinetic Mapping of Catalytic Trends. *Catal. Lett.* **2015**, *145* (3), 794–807.
- (34) Munter, T. R.; Bligaard, T.; Christensen, C. H.; Nørskov, J. K. BEP Relations for N₂ Dissociation over Stepped Transition Metal and Alloy Surfaces. *Phys. Chem. Chem. Phys.* **2008**, *10* (34), 5202–5206.
- (35) Andersen, M.; Medford, A. J.; Nørskov, J. K.; Reuter, K. Analyzing the Case for Bifunctional Catalysis. *Angew. Chem., Int. Ed.* **2016**, 55 (17), 5210–5214.
- (36) Montoya, J. H.; Tsai, C.; Vojvodic, A.; Nørskov, J. K. The Challenge of Electrochemical Ammonia Synthesis: A New Perspective on the Role of Nitrogen Scaling Relations. *ChemSusChem* **2015**, 8 (13), 2180–2186.
- (37) Kresse, G.; Furthmuller, J. Efficiency of *Ab-initio* Total Energy Calculations for Metals and Semiconductors Using a Plane-Wave Basis Set. *Comput. Mater. Sci.* **1996**, *6*, 15–50.
- (38) Kresse, G.; Hafner, J. Ab initio Molecular Dynamics for Open-Shell Transition Metals. Phys. Rev. B: Condens. Matter Mater. Phys. 1993, 48 (17), 13115–13118.
- (39) Blöchl, P. E. Projector Augmented-Wave Method. Phys. Rev. B: Condens. Matter Mater. Phys. 1994, 50 (24), 17953–17979.

- (40) Perdew, J. P.; Burke, K.; Ernzerhof, M. Generalized Gradient Approximation Made Simple. *Phys. Rev. Lett.* **1996**, *77*, 3865–3868.
- (41) Monkhorst, H. J.; Pack, J. D. Special points for Brillouin-zone integrations. *Phys. Rev. B* **1976**, *13*, 5188–5192.
- (42) Dudarev, S. L.; Botton, G. A.; Savrasov, S. Y.; Humphreys, C. J.; Sutton, A. P. Electron-Energy-Loss Spectra and the Structural Stability of Nickel Oxide: An LSDA+U Study. *Phys. Rev. B: Condens. Matter Mater. Phys.* 1998, 57, 1505–1509.
- (43) Henkelman, G.; Uberuaga, B. P.; Jónsson, H. A Climbing Image Nudged Elastic Band Method for Finding Saddle Points and Minimum Energy Paths. J. Chem. Phys. 2000, 113 (22), 9901–9904.
- (44) Henkelman, G.; Jónsson, H. A Dimer Method for Finding Saddle Points on High Dimensional Potential Surfaces Using Only First Derivatives. *J. Chem. Phys.* **1999**, *111* (15), 7010–7022.